Assessing the effect of iron oxide magnetic nanoflowers on blood components in a multi-scale approach in the context of thromboembolic disease

Monika Colombo*[A,B,‡], Yingchao Meng[B], Marie Poirier-Quinot[C], Anne-Laure Rollet[D], Audrey Geeverding[E], Andrew J deMello[B], and Ali Abou-Hassan*[D,F,‡]

A. Monika Colombo

Department of Mechanical and Production Engineering, Aarhus University, Aarhus, Denmark

B. Monika Colombo, Yingchao Meng, Andrew J deMello

Department of Chemistry and Applied Biosciences, Institute for Chemical and Bioengineering, ETH Zürich, Zürich, Switzerland.

C. Marie Poirier-Quinot

Université Paris-Saclay, CNRS, Inserm, Laboratoire d'Imagerie Biomédicale Multimodale Paris Saclay, Orsay, France

D. Ali Abou-Hassan, Anne-Laure Rollet

Sorbonne Université, CNRS, PHysico-chimie des Electrolytes et Nanosystèmes InterfaciauX, PHENIX, F-75005 Paris, France.

E. Audrey Geeverding

Sorbonne Université, CNRS, Institut de Biologie Paris-Seine (IBPS), Service de microscopie électronique (IBPS-SME), F-75005, Paris

F. Ali Abou-Hassan

Institut Universitaire de France (IUF), 75231 Paris Cedex 05, France

E-mail: mc@mpe.au.dk, ali.abou_hassan@sorbonne-universite.fr

Phone numbers: +45 22 18 98 69; + 33 1 44 27 55 18

‡ Equal contribution

Abstract word count: 147

Manuscript word count: 3871

1

Keywords: Magnetite nanoflowers, blood interaction, platelet activation, vascular diseases.

Abstract: Iron oxide magnetic nanoparticles have emerged as promising theranostic agents for cardiovascular diseases. Using a multiscale approach, we investigate the interaction of 27 nm diameter multicore magnetite nanoflowers with blood components. Using flow cytometry and dynamic light scattering, we determine safe magnetite nanoflowers concentration levels. Data indicates negligible impact on red blood cells and white blood cells for all concentrations and exposure durations studied, whilst platelets exhibit reversible activation at high magnetite nanoflowers concentrations. Magnetic resonance imaging reveals significant reductions in T1 and T2 relaxation times in platelets treated with magnetite nanoflowers at high concentrations, indicating efficient internalization. Additionally, transmission electron microscopy confirms morphological changes in platelets exposed to the iron oxide magnetic nanoparticles, indicating that internalization occurs via endocytosis. Overall, the findings support the theranostic utility of magnetite iron oxide nanoflowers in whole blood for thromboembolic disease management, with potential for future investigations over longer durations.

2

1. Background

Iron oxide magnetic nanoparticles (IONPs) have gained significant attention as theranostic agents in a range of biomedical applications, including the treatment of cardiovascular diseases.(1–5) The versatility of IONPs enables precise magnetic manipulation, drug delivery, imaging, and therapeutic interventions at both the cellular and molecular level, addressing the complex challenges posed by cardiovascular disorders.(3,6–8) Given their biocompatibility (9) and superparamagnetic properties, IONPs are primarily employed as contrast agents in magnetic resonance imaging (MRI) even in microvasculature, enhancing diagnostic capabilities.(10,11) (2,12,13) Furthermore, the utilization of IONPs in photothermal therapy has gained popularity, particularly in the context of obstructive diseases associated with blood clotting and thromboembolic events.(14) As demonstrated in cancer therapy, multicore iron oxide nanoflowers (IONFs) are able to convert absorbed near-infrared (NIR) light into heat and thus act as heat mediators in targeted photothermal therapy.(15–18)

Besides traditional application in cancer treatment, IONPs have recently been used to treat local and systemic vascular diseases, such as atherosclerosis and thrombosis.(2) IONPs can be used in hyperthermal vascular treatment to improve blood flow.(19) The potential use of IONPs for the treatment of diseases, such as thrombosis, is especially attractive when addressing regions of the microcirculation that cannot be reached using established approaches. Here, the use of nanotheranostics improves both the imaging and the treatment delivery.(20)

One of the primary concerns when using IONPs is their potential toxicity, which will vary depending on both nanoparticle structure (e.g. shape, size, surface chemistry) and dose.(21) While IONPs are generally considered to be biocompatible, excessive accumulation or prolonged exposure may lead to adverse effects, necessitating careful evaluation of their safety profiles.(22) Moreover, the susceptibility of IONPs to in vivo modifications (i.e. aggregation and degradation) can affect their magnetic properties and their theranostic efficacy, making it crucial to develop stable formulations for consistent performance.(23) For example, the hemolytic response of iron oxide has previously been assessed by exposing human red blood cells to IONPs. Such investigations have confirmed morphological changes that vary as a function of the nanoparticle concentration.(24) Moreover, loading efficiencies will depend on the nature of the targeted cells, as demonstrated by much previous research with IONPs in both cancer therapies (16,25) and vascular thromboembolic disease management.(26,27)

Herein, we leverage a multiscale physico-chemical approach to assess the interaction of IONFs with the blood components. Specifically, we use flow cytometry and magnetic resonance imaging to study primary cytocompatibility and relaxation properties to study the

3

interaction of IONFs with the biological human blood environment. Additionally, transmission electron microscopy (TEM) is used to investigate localization at the nanoscale. IONFs were chosen due to their multimodality as theranostics. Indeed, they are known to be amongst the best nanoheaters used in magnetic hyperthermia and photothermia,(16) in addition to being excellent T2 contrast agents.(18) In a theranostic context, these modalities are ideal for future applications in the imaging and treatment of cardiovascular diseases, as represented in Figure 1. Our investigations assess the interaction of IONFs with red blood cells (RBCs), white blood cells (WBCs) and platelets (PLTs) isolated from fresh human blood. The safe interaction between IONFs and human blood represents the first step of their action as nanomedicine for obstructive and thromboembolic diseases.
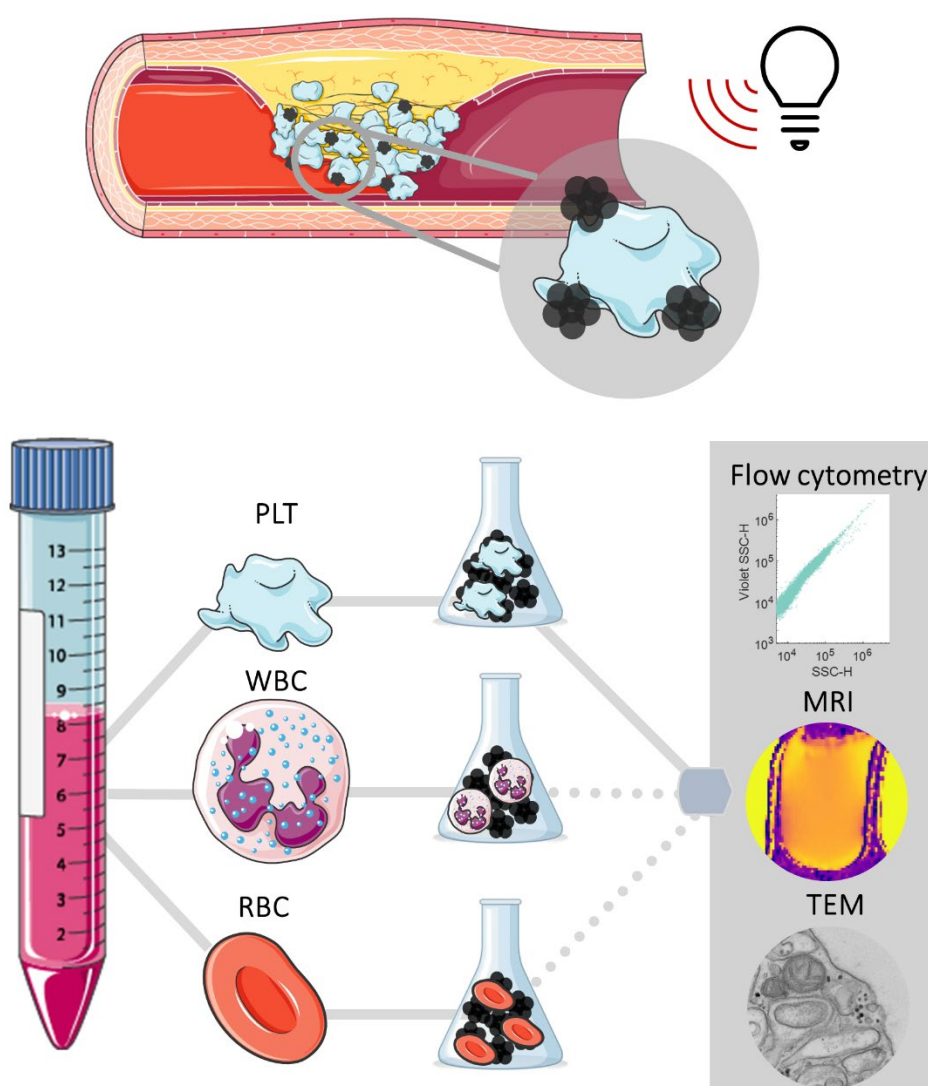
Fig. 1 – Graphical workflow showing the multi-scale approach used to study the interaction of iron oxide magnetic nanoparticles with human blood cells for future application to thromboembolic diseases. PLT: Platelet; WBC: White blood cells; RBC: Red blood cells; MRI: Magnetic resonance imaging; TEM: Transmission electron microscopy.

4

2. Methods

Preparation of the iron oxide nanoflowers

All the reagents used were of analytical purity and used as received. Nanoparticles were prepared according to a protocol developed in our previous work.(16) Ethyl acetate (>99.5%), acetone (technical grade), ethanol (96%), diethyl ether (100%), N-methyldiethanolamine (NMDEA, 99%), and diethylene glycol (DEG, 99%) were obtained from Sigma-Aldrich (Saint Quentin Fallavier, France). Sodium hydroxide (NaOH, 98%), iron(III) nitrate nonahydrate ($Fe(NO_3)_3 \cdot 9H_2O$, >98%), and iron(II) chloride tetrahydrate ($FeCl_2 \cdot 4H_2O$, 98%) were from Alfa Aesar. Iron(III) chloride hexahydrate ($FeCl_3 \cdot 6H_2O$, >97%) was obtained from Panreac (Lyon, France). The polyol process was used to prepare magnetite Fe_3O_4 nanoflowers in polyol solvents at 220°C.(11) After synthesis, IONFs were flocculated, washed and resuspended in water. To prevent IONF aggregation in physiological buffers, nanoflowers were coated with citrate. Citrate and the iron oxides were mixed in a molar ratio mol Fe/mol citrate = 0.13, and kept at 80°C for 30 minutes to promote adsorption of citrate anions onto particle surfaces.(16,36)

Dynamic light scattering measurements

Size measurements were performed using dynamic light scattering. After suspending IONFs in 1× PBS (Thermo Fisher Scientific, Reinach, Switzerland), a uniform dispersion was created by vortex mixing for 10 seconds. 200 µl samples were then filled into a micro cuvette (UV-cuvette micro, Brand, Wertheim, Germany). IONF hydrodynamic diameters were measured using a Zetasizer Nano ZS system (Malvern Instruments, Malvern, UK) operating at 20 °C in backscatter mode at optical configuration of 173°. It is noted that when particle concentrations exceed a threshold, measurement outcomes are distorted due to particle interactions. Consequently, only IONF concentrations below l00 µg Fe/mL yielded quantifiable results. The hydrodynamic diameter of each sample was assessed using the manufacturer's software (Zetasizer Nano software version 7.13, Malvern, UK). Measurements were repeated three times, before and after 5 minutes of sonication.

Fresh human blood samples

Blood samples from healthy donors were obtained from the *Blutspende Zürich* blood donation center (Schlieren, Switzerland). The study was conducted in accordance with the principles of

5

the Declaration of Helsinki, and the project was approved by the Swiss Association of Research Ethics Committees (BASEC-Nr: 2019-01721). Fresh samples were shipped in dry ice and kept at 4°C for a maximum of 48 hours. Standard protocols for the fractionation of human whole blood were followed. A commercial density-gradient medium (Lymphoprep^{TM}, STEMCELL) was used to isolate mononuclear cells. After adding it to whole blood, the solution was centrifuged at 800 g for 30 minutes. The obtained sample comprised a bottom layer of RBCs, a buffy coat consisting of suspended WBCs and PLTs, and a top layer of plasma, proteins, and PLTs. The efficacy of the fractionation protocol was verified by flow-cytometry (Figure S1). The individual components (from the top to bottom layer) were gently moved into Eppendorf cuvettes or falcon tubes according to the desired quantities for analysis.

Platelet viability protocol

PLTs were obtained after blood fractionation, yielding a PLT-rich plasma solution. To prevent mechanical activation of PLTs, further centrifugation was avoided.(37) Initial verification of PLT viability was performed using flow-cytometry. To avoid overflow, PLT-rich plasma was diluted by transferring 5 µL of solution in 295 µL of PBS in a 96-well for flow-cytometry analysis. Forward and side scatter were used to correlate signal with cell size. The final solution was prepared by mixing PLT-rich plasma in PBS at a ratio 1:3, namely 250 µL in 750 µL of PBS. Using gentle mixing to avoid activation, a homogeneous solution of PLT-rich plasma and PBS was considered for the treatment (control, distilled water, and IONFs concentrations). The treatment was added in a ratio of 1:10 of the PBS component into an Eppendorf cuvette. Following incubation of 30 minutes, 3 hours or 6 hours at room temperature, solutions were analyzed by flow-cytometry as described above. Standard gating for human blood samples was followed.(38)

Magnetic resonance imaging experiments

Experiments were performed in the BioMaps Laboratory at the University of Paris-Saclay (France). MRI experiments were performed at 3.0 T on a USA Signa^{TM} PET/MRI scanner (GE Healthcare Technologies Inc, Chicago, USA). Two rounds of experiments (T1 and T2 mapping) were performed after an incubation period of 30 minutes for the IONFs-C$_1$ and IONFs-C$_3$ samples.(39) T1 mapping was performed using an inversion recovery sequence with 6 values of inversion recovery time (50, 200, 300, 600, 1000 and 1977 ms), an echo time of 11 ms, a repetition time of 2000 and an acquisition time of 3 minutes. T2 mapping followed a GE dedicated sequence, with 16 echo times varying between 8.9 and 142 msec, a repetition time of

6

1200 and an acquisition time of 3:15 minutes. T1 and T2 values were measured at three regions of interest (ROIs) located at the top, middle and bottom of the sample. This was done to account for the effect of gravity and sedimentation on the blood sample.

Transmission electron microscopy

The blood PLTs were fixed with 1.5 % glutaraldehyde and 1 % PFA in 0.1 M cacodylate buffer (pH 7.4) overnight at 4°C. Further steps were assisted with a Pelco Biowave Pro+ (Ted Pella) microwave device: 3 buffer washes with cacodylate buffer 0.1 M (200 W 40 s), 0.2 % OTE in 0.1 M cacodylate buffer (150 W ON/OFF/ON cycles 7 x 2 min), 3 buffer washes with cacodylate buffer 0.1 M (200 W 40 s), 1 % osmium tetroxide in 0.1 M cacodylate buffer (100 W ON/OFF/ON cycles 7 x 2 min) and 3 deionized water washes (200 W 40 s). PLTs were pre-embedded with 4 % agarose in deionized water, dehydrated through a graded concentration of ethanol 50-70-95-100-100 % then acetone 100-100 % (200 W 40 s), infiltrated with a graded concentration of acetone and Epon resin mix 10-25-50-75-90 % and 3 times with 100 % Epon resin (200 W 5 min). Resin infiltration steps were performed under vacuum (20 mm Hg). Samples were embedded in silicone mold with resin and polymerized at 60° C for 72 hours. 70 nm ultrathin sections were cut with an Ultracut ultramicrotome (UCT, Leica microsystems), deposited on 150 mesh copper grids, and contrasted with 2.5 % uranyl acetate and 2 % lead citrate. Observations were performed using a LaB6 JEM 2100 HC TEM (Jeol) at 80 kV. Acquisitions were made with a side mounted Veleta CCD camera driven by iTEM software version 5.2 (Olympus, Japan). Images were recorded with a 2k x 2k pixels definition (binning 1x1) and a 750 ms exposure time.

Statistical analysis

The biological assays were repeated in triplets for two individual donors. The relaxation times were measured independently in three different sample regions. Data are shown as means ± standard deviation, following a normality test. Statistical significance was accepted for *p*-values < 0.01. Given the normal distribution of the data, parametric paired *t*-test and ANOVA tests were conducted. All analyses were performed in MATLAB (MathWorks, Natick, MA, USA) and Origin (OriginLab Corporation, Northampton, MA, USA). Flow-cytometry data were analyzed using FlowJo software (FlowJo LLC, Ashlan, OR, USA).

3. Results and Discussion

3.1 Nanoflower characterization

Figure 2-A presents a representative TEM image of the synthesized iron oxide nanoparticles, showcasing their multicore nanoflower morphology. The IONFs have an average diameter, d_0, of 27 nm and a standard deviation, σ, of 0.1, as deduced from the size histogram fitted to a log-normal model (Figure 2-B). Next the IONF concentration range was assessed, based on prior literature and clinical utility. Studies by Andreas et al. indicated that low toxicity was found for nanoparticle concentrations below 100 µg Fe/mL. (28) Accordingly, we defined the treatment conditions reported in Table 1.
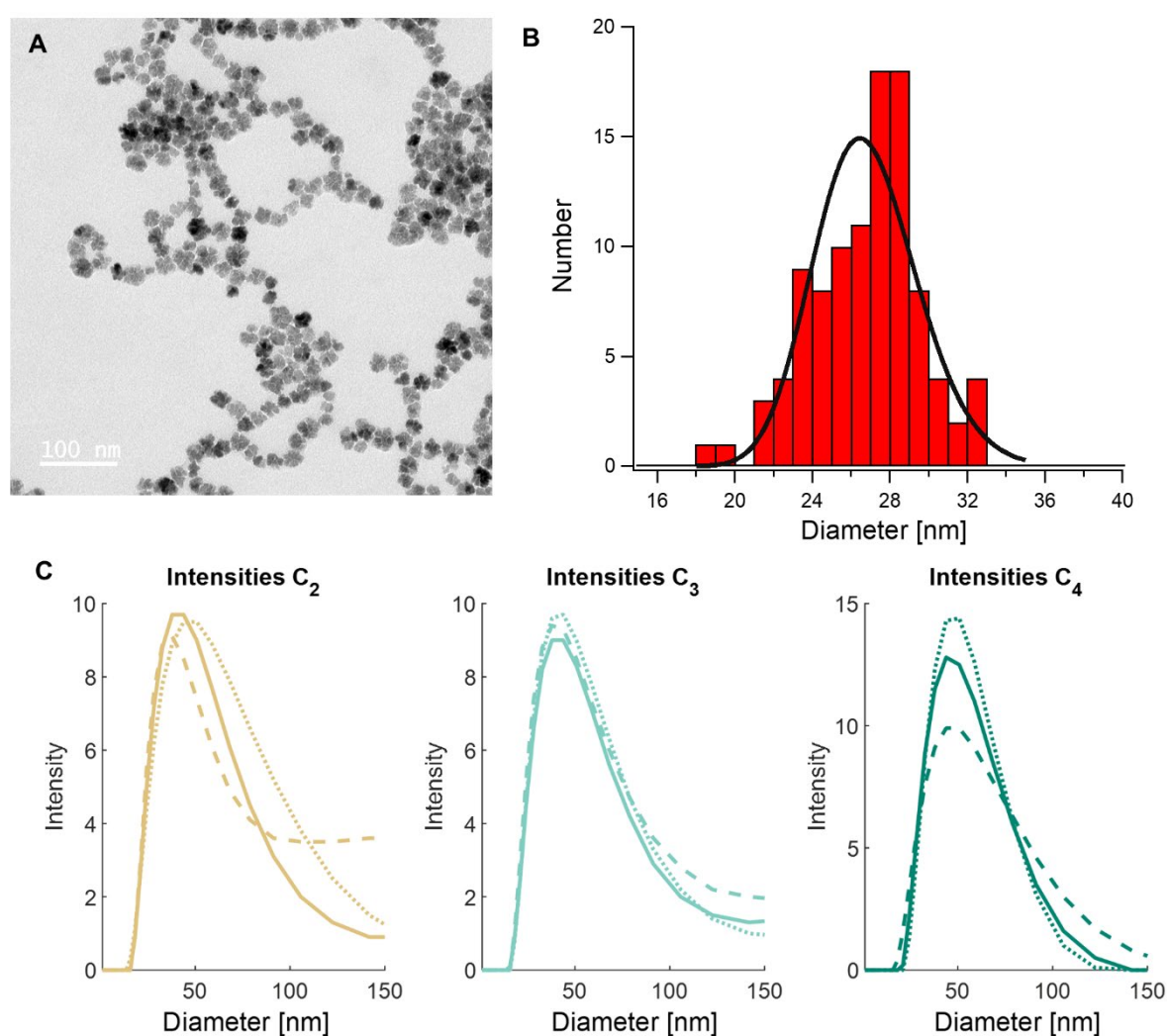
Fig. 2 - Preparation and characterization of iron oxide nanoflowers (IONFs). A) Transmission electron microscopy image of multicore IONFs; B) Size distribution histogram of IONFs fitted to a Log-Normal law and C) Dynamic light scattering size distribution analysis based on intensity for different IONFs suspensions in PBS.

8

Table 1 – Molar and mass concentrations of all IONFs suspensions in PBS investigated in this work.

Sample	Molar concentration (μM)	Mass concentration (μg Fe/mL)
control	0	0
C_1	1.79×10^3	100
C_2	179.0	10
C_3	17.90	1
C_4	1.79	0.1

Sample solutions were obtained by serial dilution in phosphate buffer saline (PBS) from a stable suspension of citrated IONFs in water, having a Fe concentration of 32.1 mM. Dynamic light scattering of the diluted solutions indicated limited IONF agglomeration, with hydrodynamic diameters ranging between 37.8 and 43.8 nm.

3.2 A low dose of IONFs can induce reversible platelet activation

After ensuring correct fractionation of whole blood through flow-cytometry analysis (Figure S1), each blood component was investigated using appropriate protocols and methodologies as detailed in the following section. Briefly, RBC interactions with IONFs were examined by quantifying the total rate of hemolysis after exposure of 30 minutes, 3 hours and 6 hours.[29] The rate of hemolysis (i.e. the release of hemoglobin) was negligible even when using the highest IONF concentration (Figure S2). This suggests that RBCs are negligibly affected by exposure to the IONFs at the selected concentrations. The interaction of WBCs with IONFs was assessed using flow-cytometry. Again, a negligible shift in the fluorescence distribution indicates that WBCs are not affected by the presence of IONFs to an appreciable extent (Figure S3).

PLT viability after incubation and exposure to IONFs was also assessed through flow-cytometry. A control group was considered along with samples at four different IONF concentrations, and incubation times of 30 minutes, 3 hours, and 6 hours. Figure 3 presents violet side scatter vs. side scatter plots of PLTs incubated for 30 minutes. It can be seen that a sub-population (shifted to higher intensities) grows as a function of IONF concentration. This sub-population is also seen to diminish as a function of incubation times (Figure S4). Analysis of a IONFs-C_1 solution smear under light microscopy (Figure 3-B), confirmed that PLTs tend to spread as pseudopods that can extend over several micrometers from the PLT.[30] As

9

expected, analysis of the control solution indicated no pseudopod formation. For this reason, and in agreement with previous studies on PLTs, the side formation in the scatter plots was associated with morphologically changed platelets (i.e. activation induced by IONFs).

We next compared the frequency gating of the forward scatter data of the PLT baseline control condition (t_0) with the PLTs incubated with IONFs-C_1 for 30 minutes, 3 hours and 6 hours (Figure 3-C and Figure S5). It is notable that in case of the 30-minute incubation the trend of the frequency ratios, gated on the histogram plots of forward scattering, is opposite to that of baseline condition. Specifically, the fr_2 frequency gate is smaller than the fr_3 frequency gate for 30-minute incubation, whereas fr_2 is larger than fr_3 for the baseline condition. However, for longer incubation times, the frequency trend is similar to that of the baseline, confirming that PLT activation is limited in time and that exposure to IONFs-C_1 does not induce PLT apoptosis.
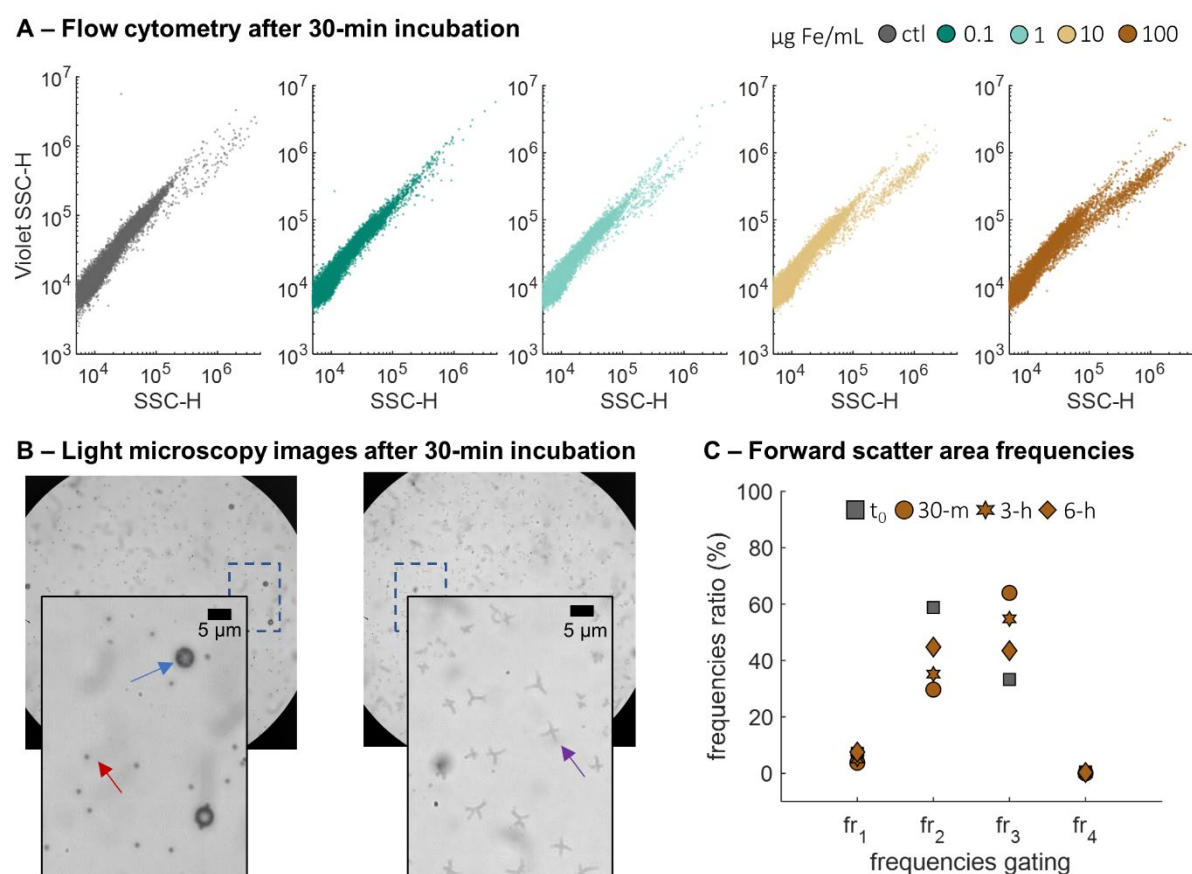

Fig. 3 – Biological characterization of IONFs after 30 minutes incubation with isolated platelets suspended in plasma. A) Side scatter flow cytometry plots. B) Brightfield microscopy images of a plasma smear sample after a 30-minute incubation of the control and C1 treatment. The round black dots in (B) are identified as viable, non-activated PLTs (red arrow). Reference 5-μm polystyrene beads are also shown (blue arrow). Structures resembling PTLs pseudopods are indicated by the purple arrow. C) Comparison of the frequencies of the forward scatter data of the PLTs baseline untreated condition (t0, grey square) and PLTs incubated with IONFs-C1 for 30 minutes (brown circle), 3 hours (brown hexagram), and 6 hours (brown diamond).

10

3.3 Interaction of IONFs with PLT at high concentration induces changes in MRI relaxivities

Since the MRI contrast (and relaxation times) effect produced by the IONPs depends on multiple parameters, including the local environment, relaxation times can be used to report nanoscale local effects. To quantify such changes, we measured the longitudinal (T1) and transverse (T2) relaxation times once the IONFs are mixed with the different blood cells at 0, 30, 45, and 65 minutes, Figure 4.[31] Previous results have established the excellent function of IONFs as negative MRI contrast agents (T2-agents) showing an r_2 relaxivity of about 656.8 mM^{-1} s^{-1} in water and a r_1 relaxivity of approximately 10.16 mM^{-1} s^{-1} at 3T.[18]

IONFs were contacted with RBCs and PLTs (for IONFs-C$_1$ and IONFs-C$_3$) and MRI images acquired at different times to extract T1 and T2 relaxation times. Figure 4-A presents relaxation maps for both RBC and PLT controls and IONFs-C$_1$ treated solutions. The dual maps of RBCs and PLTs treated with IONFs-C$_3$ are provided in Figure S6. For both concentrations, relaxation times of all the solutions were relatively constant over the considered time span. We then quantified the T1 and T2 relaxation times in three different ROIs in the sample, considering the effects of gravity on RBC sedimentation over time. It is worth noting that T1 relaxations times for the RBC control and with IONFs-C$_3$ varied for the three measurements, indicating a gravitational effect and consequent sedimentation (Table S2). For example, for 30 minutes, in the same ROI, the addition of the IONFs to RBCs and PLTs induced a decrease in T1 and T2 relaxation times. Indeed, T1 relaxation times of the solutions of RBCs (691.60 ± 6.56 ms) and PLTs (675.76 ± 5.76 ms) with IONFs-C$_1$ (Figure 4-A and Table S1) were statistically different from the RBC (816.73 ± 1.79 ms) and PLTs (834.26 ± 1.83 ms) controls, with *p*-values of 0.00053 and 0.00034, respectively. In the case of IONFs-C$_3$, no statistical difference was seen for the T1 relaxation time when added to either RBCs or PLTs (with *p*-values of 0.42 and 0.04, respectively). Namely, the T1 relaxation time for RBCs (826.40 ± 1.73 ms) and PLTs (831.57 ± 2.82 ms) with IONFs-C$_3$ were comparable to the RBC (827.90 ± 2.31 ms) and PLT (838.76 ± 0.37 ms) controls. When considering the T2 relaxation times (Table S3-4), data indicate a more significant impact. Indeed, values for RBCs (27.59 ± 1.01 ms) and PLTs (18.59 ± 0.26 ms) incubated for 30 minutes with IONFs-C$_1$ were statistically different to the RBC (215.64 ± 11.50 ms) and PLT (542.79 ± 12.77 ms) controls, with *p*-values of 0.0013 and 0.00021, respectively (Figure 4-B, Table S3). Conversely, for the lower concentration IONFs-C$_3$, no statistical differences in T2 relaxation time were found for RBCs (285.85 ± 20.68 ms) and PLTs (419.80 ± 9.46 ms) when compared to the control RBC (314.01 ± 49.92 ms) and PLT (418.91

11

± 18.10 ms) solutions (*p*-value of 0.24 and 0.87, respectively). These results indicate that for the C1 concentration nanoparticles may undergo clustering and cell internalization, leading to a decrease in T1 and T2, respectively. Such a concentration-dependent clustering is in agreement with the DLS results (Figure. 2). In addition, and despite the low concentration of C1, nanoparticles can still induce a significant reduction in both longitudinal T1 and transverse T2, confirming their function as effective MRI contrast agents.
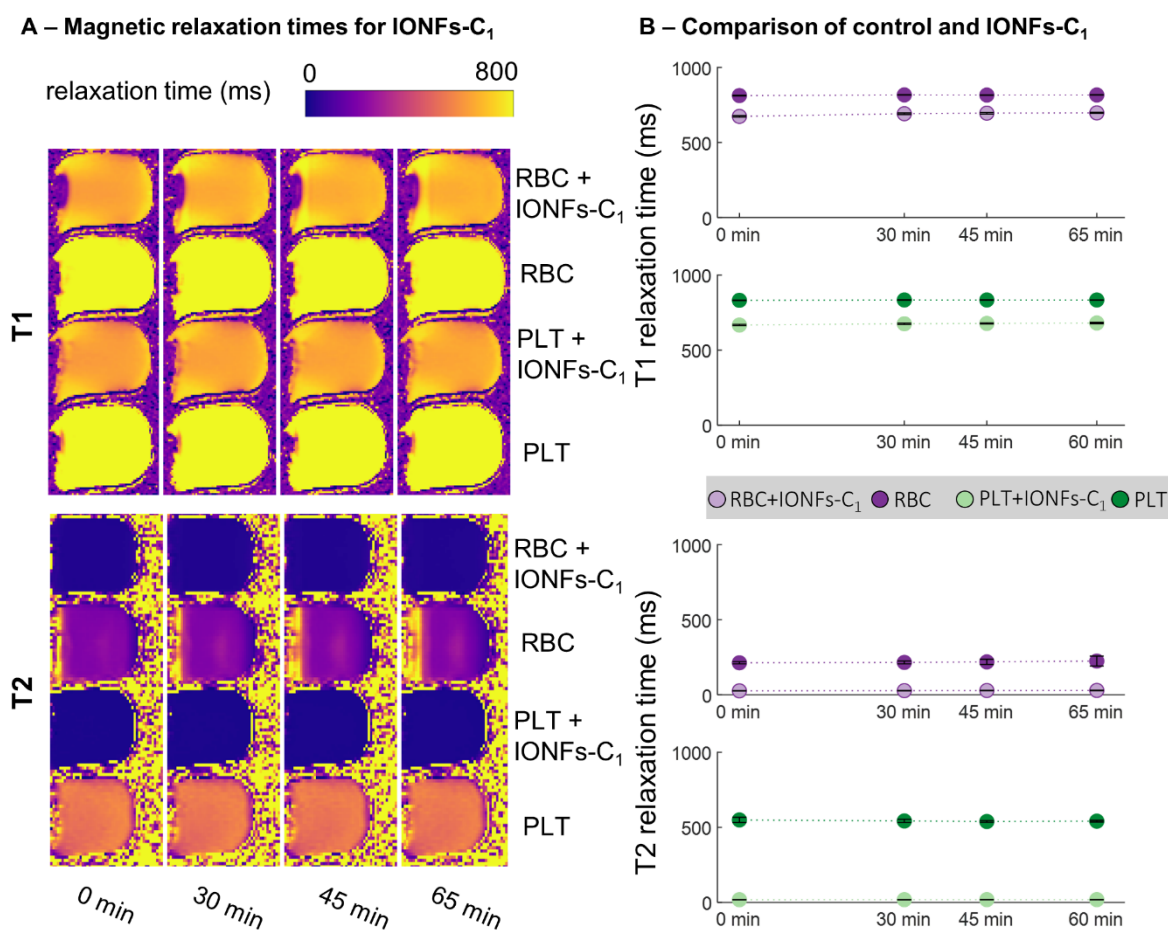

Fig. 4 – Magnetic activity of iron oxide nanoflowers after a 30-minute incubation with red blood cells and platelets. A) T1 (top) and T2 (bottom) relaxation maps for the RBC and PLT control and incubated for 30 minutes with IONFs-C1. B) Quantitative comparison of the T1 (top) and T2 (bottom) measurements across 3 regions of interest for each time point (0, 30, 45 and 65 minutes) for all the considered solutions (control and IONFs-C1 treatment).

3.4 IONFs are internalized in PLTs at high concentration

To assess the localization of the IONFs once in contact with PLTs and the morphological changes that they may induce, we acquired TEM images of PLTs exposed to IONFs-C_1 and IONFs-C_3 concentrations and control for 30 minutes. Images at different magnifications were

12

analyzed as shown in Figure 5, where the α-granules typical of PLTs could be observed.(30,32)
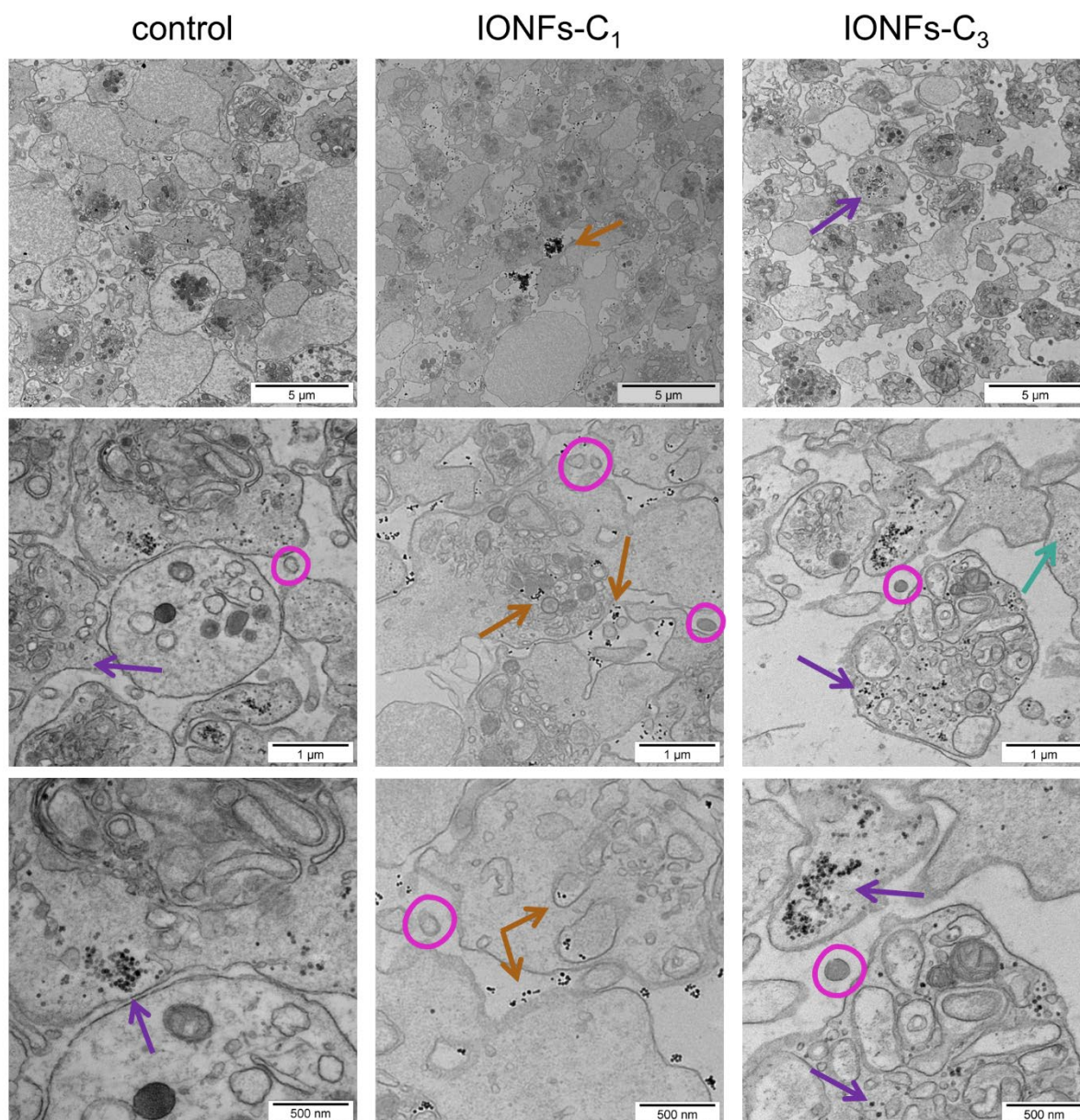
Fig. 5 – Images at different magnifications obtained by transmission electron microscopy of PLT-rich plasma in the case of control, C1 and C3 nanoflowers concentrations, after a 30-minute incubation Scale bars indicate (top to bottom): 5 μm, 1 μm and 500 nm. Glycogen (purple arrow); IONFs (brown – C1 - and turquoise – C3 - arrows); ectosome-like formations (pink circles). (30,33,35)

In agreement with previous studies, it was possible to identify in both the control and IONFs-C_3 an abundance of glycogen granules (spheroidal formations about 50 nm in size) contained within the PLT cytoplasm.(30,33) It is observed that in case of IONFs-C_1, glycogen agglomerations were less abundant or barely identifiable. Glycogen is indeed known to serve as reservoir for energy production in PLTs; during PLT activation (a transition from low-energy resting states to high-demanding metabolic states) glycogen is degraded through

13

glycogenolysis.(33,34) In the case of IONFs-C_1, individual or aggregated IONFs were seen both in the extracellular and intracellular environment, as indicated by brown arrows. This suggests that the IONFs-C_1 has induced transition to a high-demanding state where the stored glycogen is engaged.(30,33) Furthermore, we concluded that IONFs-C_1 at 30 minutes were possibly internalized by endocytosis.

From the morphological viewpoint, when exposed to IONFs-C_1, PLTs generally showed a more elongated shape when compared to the control and IONFs-C_3 samples from the same blood sample and for the same incubation time. As shown in Figure S7, at higher magnification the typical flower-shape IONFs could be observed and were abundant in the extracellular environment. After 30 minutes incubation with IONFs-C_3, no major IONF aggregation was detectable in extracellular or intracellular environments, where an abundance of particulate matter (50-60 nm in size) related to glycogen was found. Only a few IONFs could be identified (as indicated by the turquoise arrow). Finally, vesicular formation referable to ectosomes could be visualized in the case of IONFs-C_1, and in lower amount, of IONFs-C_3 and control (indicated by pink circles).(35) To conclude, TEM images confirmed the biological data as well as the hypothesis that IONFs-C_1 concentration can induce notable alterations to PLTs, while undergoing clustering, membrane interaction and internalization.

4. Conclusion

We have investigated the interaction of iron oxide nanoflowers with blood components, focusing on the primary biological changes of PLTs. By employing fresh human blood, we selected different IONFs concentration levels, and studied the effects on RBCs, WBCs and PLTs. From the biological standpoint, only PLTs were appreciably affected by incubation with the highest IONFs concentration for 30 minutes. This activation, however, disappeared after further incubation. Conversely, RBC and WBC homeostasis were not affected at any incubation time or at any IONFs concentration. From MRI measurements, a substantial reduction of the T1 and T2 relaxation times for IONFs-C_1 was seen when compared to the control cases in both PLT and RBC populations. Lower concentrations of IONFs (IONFs-C_3) induced negligible effects compared to the control. Finally, TEM images showed that PLT-rich plasma exposed to IONFs-C_1 could internalize IONFs within PLTs. Accordingly, we conclude that IONF concentrations close to C_1 in human blood can induce temporary morphological changes in PLTs. These results show that the selected IONFs may be promising candidates for further theranostic applications in whole blood for thromboembolic diseases.

14

Acknowledgements

Author contributions

M.C: Conceptualization; Data curation; Formal analysis; Investigation; Methodology; Project administration; Writing - original draft; and Writing - review & editing.

Y.M: Investigation; Methodology; and Writing - review & editing.

M.P.-Q: Investigation; Methodology; Writing - original draft; and Writing - review & editing.

A.-L.R: Methodology, Writing - review & editing.

A.G: Investigation, Writing - review & editing.

A.J.dM: Funding acquisition; Resources; Supervision; Writing - review & editing

A.A.-H: Conceptualization; Formal analysis; Funding acquisition; Investigation; Methodology; Project administration; Resources; Supervision; Writing - original draft; and Writing - review & editing.

Conflict of Interest

The authors declare no conflict of interest.

References

1. Younis NK, Ghoubaira JA, Bassil EP, Tantawi HN, Eid AH. Metal-based nanoparticles: Promising tools for the management of cardiovascular diseases. Nanomedicine: Nanotechnology, Biology and Medicine. 2021 Aug 1;36:102433.

2. Vazquez-Prada KX, Lam J, Kamato D, Xu ZP, Little PJ, Ta HT. Targeted Molecular Imaging of Cardiovascular Diseases by Iron Oxide Nanoparticles. Arteriosclerosis, Thrombosis, and Vascular Biology. 2021 Feb;41(2):601–13.

3.   Omidian H, Babanejad N, Cubeddu LX. Nanosystems in Cardiovascular Medicine: Advancements, Applications, and Future Perspectives. Pharmaceutics. 2023 Jul 12;15(7):1935.

4.   Cazares-Cortes E, Wilhelm C, Efrain Perez J, Espinosa A, Casale S, Michel A, et al. Tuning the load of gold and magnetic nanoparticles in nanogels through their design for enhanced dual magneto-photo-thermia. Chemical Communications. 2021;57(48):5945–8.

5.   Cazares-Cortes E, Cabana S, Boitard C, Nehlig E, Griffete N, Fresnais J, et al. Recent insights in magnetic hyperthermia: From the "hot-spot" effect for local delivery to combined magneto-photo-thermia using magneto-plasmonic hybrids. Advanced Drug Delivery Reviews. 2019 Jan 1;138:233–46.

6.   Serio F, Silvestri N, Kumar Avugadda S, Nucci GEP, Nitti S, Onesto V, et al. Co-loading of doxorubicin and iron oxide nanocubes in polycaprolactone fibers for combining Magneto-Thermal and chemotherapeutic effects on cancer cells. Journal of Colloid and Interface Science. 2022 Feb 1;607:34–44.

7.   Fernandes S, Fernandez T, Metze S, Balakrishnan PB, Mai BT, Conteh J, et al. Magnetic Nanoparticle-Based Hyperthermia Mediates Drug Delivery and Impairs the Tumorigenic Capacity of Quiescent Colorectal Cancer Stem Cells. ACS Appl Mater Interfaces. 2021 Apr 14;13(14):15959–72.

8.   Demri N, Dumas S, Nguyen ML, Gropplero G, Abou-Hassan A, Descroix S, et al. Remote Magnetic Microengineering and Alignment of Spheroids into 3D Cellular Fibers. Advanced Functional Materials. 2022;32(50):2204850.

9.   Arias LS, Pessan JP, Vieira APM, de Lima TMT, Delbem ACB, Monteiro DR. Iron Oxide Nanoparticles for Biomedical Applications: A Perspective on Synthesis, Drugs, Antimicrobial Activity, and Toxicity. Antibiotics (Basel). 2018 Jun 9;7(2):46.

10.   Khurshid H, Friedman B, Berwin B, Shi Y, Ness DB, Weaver JB. Blood clot detection using magnetic nanoparticles. AIP Adv [Internet]. 2017 Feb 16 [cited 2018 Nov 1];7(5). Available from: https://www.ncbi.nlm.nih.gov/pmc/articles/PMC5315662/

11.   Karagkiozaki V, Pappa F, Arvaniti D, Moumkas A, Konstantinou D, Logothetidis S. The melding of nanomedicine in thrombosis imaging and treatment: a review. Future Sci OA [Internet]. 2016 Mar 23 [cited 2018 Nov 1];2(2). Available from: https://www.ncbi.nlm.nih.gov/pmc/articles/PMC5138016/

12.   Rahman M. Magnetic Resonance Imaging and Iron-oxide Nanoparticles in the era of Personalized Medicine. Nanotheranostics. 2023 Aug 21;7(4):424–49.

13.   Abdel-Mageed HM, AbuelEzz NZ, Radwan RA, Mohamed SA. Nanoparticles in nanomedicine: a comprehensive updated review on current status, challenges and emerging opportunities. Journal of Microencapsulation. 2021 Aug 18;38(6):414–36.

14.   Pala R, Pattnaik S, Busi S, Nauli SM. Nanomaterials as Novel Cardiovascular Theranostics. Pharmaceutics. 2021 Mar 7;13(3):348.

16

15. Zou L, Wang H, He B, Zeng L, Tan T, Cao H, et al. Current Approaches of Photothermal Therapy in Treating Cancer Metastasis with Nanotherapeutics. Theranostics. 2016 Mar 21;6(6):762–72.

16. Cabana S, Curcio A, Michel A, Wilhelm C, Abou-Hassan A. Iron Oxide Mediated Photothermal Therapy in the Second Biological Window: A Comparative Study between Magnetite/Maghemite Nanospheres and Nanoflowers. Nanomaterials. 2020 Aug;10(8):1548.

17. Walle AV de, Figuerola A, Espinosa A, Abou-Hassan A, Estrader M, Wilhelm C. Emergence of magnetic nanoparticles in photothermal and ferroptotic therapies. Materials Horizons. 2023;10(11):4757–75.

18. Benassai E, Hortelao AC, Aygun E, Alpman A, Wilhelm C, Saritas EU, et al. High-throughput large scale microfluidic assembly of iron oxide nanoflowers@PS-b-PAA polymeric micelles as multimodal nanoplatforms for photothermia and magnetic imaging. Nanoscale Adv. 2023 Dec 19;6(1):126–35.

19. Gao W, Sun Y, Cai M, Zhao Y, Cao W, Liu Z, et al. Copper sulfide nanoparticles as a photothermal switch for TRPV1 signaling to attenuate atherosclerosis. Nature Communications. 2018 Jan 15;9(1):231.

20. Russell P, Hagemeyer CE, Esser L, Voelcker NH. Theranostic nanoparticles for the management of thrombosis. Theranostics. 2022 Mar 14;12(6):2773–800.

21. Patil US, Adireddy S, Jaiswal A, Mandava S, Lee BR, Chrisey DB. In Vitro/In Vivo Toxicity Evaluation and Quantification of Iron Oxide Nanoparticles. Int J Mol Sci. 2015 Oct 15;16(10):24417–50.

22. Arami H, Khandhar A, Liggitt D, Krishnan KM. In vivo delivery, pharmacokinetics, biodistribution and toxicity of iron oxide nanoparticles. Chem Soc Rev. 2015 Dec 7;44(23):8576–607.

23. Pucci C, Degl'Innocenti A, Gümüş MB, Ciofani G. Superparamagnetic iron oxide nanoparticles for magnetic hyperthermia: recent advancements, molecular effects, and future directions in the omics era. Biomaterials Science. 2022;10(9):2103–21.

24. Agarwal V, Gupta V, Bhardwaj VK, Singh K, Khullar P, Bakshi MS. Hemolytic Response of Iron Oxide Magnetic Nanoparticles at the Interface and in Bulk: Extraction of Blood Cells by Magnetic Nanoparticles. ACS Appl Mater Interfaces. 2022 Feb 9;14(5):6428–41.

25. Kaushik S, Thomas J, Panwar V, Ali H, Chopra V, Sharma A, et al. In Situ Biosynthesized Superparamagnetic Iron Oxide Nanoparticles (SPIONS) Induce Efficient Hyperthermia in Cancer Cells. ACS Appl Bio Mater. 2020 Feb 17;3(2):779–88.

26. Cabrera D, Eizadi Sharifabad M, Ranjbar JA, Telling ND, Harper AGS. Clot-targeted magnetic hyperthermia permeabilizes blood clots to make them more susceptible to thrombolysis. Journal of Thrombosis and Haemostasis. 2022 Nov 1;20(11):2556–70.

27. Jia JM, Chowdary PD, Gao X, Ci B, Li W, Mulgaonkar A, et al. Control of cerebral ischemia with magnetic nanoparticles. Nature Methods. 2017 Feb;14(2):160–6.

28. Andreas K, Georgieva R, Ladwig M, Mueller S, Notter M, Sittinger M, et al. Highly efficient magnetic stem cell labeling with citrate-coated superparamagnetic iron oxide nanoparticles for MRI tracking. Biomaterials. 2012 Jun 1;33(18):4515–25.

29. Zijlstra WG, Buursma A. Spectrophotometry of Hemoglobin: Absorption Spectra of Bovine Oxyhemoglobin, Deoxyhemoglobin, Carboxyhemoglobin, and Methemoglobin. Comparative Biochemistry and Physiology Part B: Biochemistry and Molecular Biology. 1997 Dec 1;118(4):743–9.

30. Swanepoel AC, Pretorius E. Ultrastructural analysis of platelets during three phases of pregnancy: A qualitative and quantitative investigation. Hematology. 2015 Jan 1;20(1):39–47.

31. Rosmini S, Bulluck H, Abdel -Gadir Amna, Treibel TA, Culotta V, Thompson R, et al. The Effect of Blood Composition on T1 Mapping. JACC: Cardiovascular Imaging. 2019 Sep;12(9):1888–90.

32. Blair P, Flaumenhaft R. Platelet α–granules: Basic biology and clinical correlates. Blood Rev. 2009 Jul;23(4):177–89.

33. Prakhya KS, Vekaria H, Coenen DM, Omali L, Lykins J, Joshi S, et al. Platelet glycogenolysis is important for energy production and function. Platelets. 2023 Dec 31;34(1):2222184.

34. Whiteheart SW. Fueling platelets: Where does the glucose come from? Arterioscler Thromb Vasc Biol. 2017 Sep;37(9):1592–4.

35. De Paoli SH, Tegegn TZ, Elhelu OK, Strader MB, Patel M, Diduch LL, et al. Dissecting the biochemical architecture and morphological release pathways of the human platelet extracellular vesiculome. Cell Mol Life Sci. 2018 Oct 1;75(20):3781–801.

36. Massart R. Preparation of aqueous magnetic liquids in alkaline and acidic media. IEEE Transactions on Magnetics. 1981 Mar;17(2):1247–8.

37. Söderström AC, Nybo M, Nielsen C, Vinholt PJ. The effect of centrifugation speed and time on pre-analytical platelet activation. Clinical Chemistry and Laboratory Medicine (CCLM). 2016 Dec 1;54(12):1913–20.

38. Rico LG, Salvia R, Ward MD, Bradford JA, Petriz J. Flow-cytometry-based protocols for human blood/marrow immunophenotyping with minimal sample perturbation. STAR Protoc. 2021 Oct 11;2(4):100883.

39. Vidmar J, Serša I, Kralj E, Tratar G, Blinc A. Discrimination between red blood cell and platelet components of blood clots by MR microscopy. Eur Biophys J. 2008 Sep 1;37(7):1235–40.